Earth Planet. Sci. Lett. 675 (2026) 119790

Contents lists available at ScienceDirect

Earth and Planetary Science Letters

journal homepage: www.elsevier.com/locate/epsl

# Using rate-and-state friction constitutive laws to predict seismicity rates for ice rifts on the Ross Ice Shelf in Antarctica

Kathrine Udell-Lopez *, Mong-Han Huang, Vedran Lekić

*Department of Geology, University of Maryland, College Park, USA*

ARTICLE INFO

Editor: J.P. Avouac

*Keywords:*
Seismology
Glaciology
Seismicity rate
Rate-and-state friction
Tidal stress
Periodic seismicity

ABSTRACT

Determining what fault characteristics and applied stress conditions modulate the occurrence of seismicity is a key question in the field of seismology. Here we analyze the seismicity measured at two ice shelf rift zones of different maturity in the Ross Ice Shelf, which are subjected to long-term dilatational stress modulated by tidal stress variations. We analyze the periodicity of the seismicity and its relationship to tidal stress variations and find that the seismicity rate at both rifts is controlled by tidal stress rate variations. We compare the observed icequake occurrence times with analytical predictions from rate-and-state friction constitutive laws that have been used to model frictional behavior on terrestrial faults. We find that seismicity rate is predicted well by an analytical model based on rate-and-state friction, confirming that it can be used to understand ice rift seismicity. We constrain for the first time the characteristic time of seismicity rate, $t_a$, for both rifts, and find that ice rifts have a faster recovery time than continental faults, and that their responses to stress and characteristic times are age dependent. This implies that the strength of the rift changes with time and determines the amount of stress or stress rate dependency of the system. Our results can be used to understand seismicity occurrence across other ice rifts in Antarctica and Greenland and holds implications for seismicity on icy satellites.

## 1. Introduction

Understanding the brittle failure process is essential to both the fields of seismology and glaciology. For seismology, brittle failure is important in the context of earthquake and fault zone processes. In glaciology, much of the processes of ice shelf collapse and iceberg calving are assumed to occur through brittle failure during relatively short time periods (Alley et al., 2023; Olinger et al., 2024; Rist et al., 1999; Scambos et al., 2009). Therefore, understanding potential time-evolution of brittle fracture of ice can inform predictions of integrity of ice shelves under future climate conditions. In terrestrial seismology, brittle failure observed through earthquakes has been successfully described using models in which friction on a fault depends on the slip rate and a history-dependent state variable (Dieterich, 1994, 1992; Heimisson and Segall, 2018). This model relates the statistical observation of Omori's aftershock decay law (duration of aftershock production following a large event) with fault slip experimental observations (applied stresses and fault friction) (Dieterich, 1994, 1987, 1986).

Under the rate-and-state framework, a characteristic time, $t_a$, describes the characteristic timescale on which the aftershock production rate returns to the background seismicity rate (Ader and Avouac, 2013; Dieterich, 1994, 1992). In the context of earthquake slip against friction, the $t_a$ can also be related to the ratio of normal stresses to the background Coulomb stress rate by:

$$t_a = \frac{A\sigma_0}{\dot{s}_0}, \tag{1}$$

where $\sigma_0$ is initial normal stress, and $\dot{s}_0$ is the rate of change of background stress (Dieterich, 1994), and $A$ is a constitutive parameter proportional to the instantaneous frictional dependence on slip rate (Beeler et al., 2022; Dieterich and Kilgore, 1996, 1994). Because fault age and material properties both influence $A$, it is not typically possible to predict its value from available information; instead, observationally constraining $t_a$ can inform us about properties of inaccessible faults.

One way of attempting to observationally constrain $t_a$ is by studying the recurrence interval of main shocks. This is because the characteristic time ($t_a$) is thought to be proportional to the recurrence interval, as it is related to both initial normal stress clamping a fault and the background stress rate that will eventually cause the fault to slip (Dieterich, 1994).

* Corresponding author.
*E-mail address:* kudell@umd.edu (K. Udell-Lopez).

https://doi.org/10.1016/j.epsl.2025.119790
Received 6 May 2025; Received in revised form 7 November 2025; Accepted 12 December 2025
Available online 17 December 2025

However, this approach is made difficult by the inadequate duration of observational historic records compared to the often-long time periods between major earthquake events (Parsons, 2002; Perfettini and Avouac, 2004; Stein and Liu, 2009).

Periodic seismicity caused by oscillatory stresses such as tides or seasonal loading offers an alternative way of constraining $t_a$. This is because it implies a repetitive process that fully encapsulates the earthquake cycle and places constraints on initiation, rupture, aftershock, and resetting of stress conditions. The characteristics of this periodic seismicity carry information about how quickly a fault can re-rupture, the strength of the fault, its frictional properties, and the level of stress required to fracture it, i.e. all the parameters that go into calculating $t_a$. Oscillatory stresses such as tides or seasonal loading of snow/water have been shown to produce periodic seismicity in a variety of locations (Cochran et al., 2004) including California (Beaucé et al., 2023; Bucholc and Steacy, 2016; Johnson et al., 2017; Thomas et al., 2012, 2009), Japan (Ueda et al., 2024), the Himalayas (Ader and Avouac, 2013; Bettinelli et al., 2008), Taiwan (Hsu et al., 2021), and several faults in oceanic plates (Lordi et al., 2022; Tolstoy et al., 2002).

Recently, Heimisson and Avouac (2020) suggested that under oscillatory stresses ($S_T$), whether a system's seismicity rate is modulated by stress ($S_T$) or stress rate ($\dot{S}_T$) is determined by the value of $t_a$ relative to the oscillating stress periodicity, $T$. This conclusion was drawn from a modification to the general form of the rate-and-state equation by Heimisson and Segall (2018):

$$R(t) = r\frac{K(t)}{1 + \frac{1}{t_a}\int_0^t K(\tau)d\tau}, \tag{2}$$

where $R(t)$ is the seismicity rate (number of events per unit time) produced by a population of seismic sources with background seismicity rate $r$ (total number of events divided by total duration). If changes in normal stress, $\sigma(t)$, are small compared to initial normal stress, $\sigma_0$, then $K(t)$ can be approximated as (as explained by Heimisson and Segall, 2018):

$$K(t) \approx \exp\left(\frac{S(t)}{A\sigma_0}\right), \tag{3}$$

where $S(t)$ is the modified Coulomb stress history and can be written as a combination of short term periodic oscillatory stresses and long-term stress rate:

$$S(t) = S_T(t) + \dot{s}_0 t. \tag{4}$$

Eq. (2) relates the periodic seismic event rate, R(t), to the combined effects of oscillatory Coulomb stresses ($S_T$), background Coulomb stresses ($\dot{s}_0$), frictional properties ($A$), and the characteristic time ($t_a$). Notably, when $t_a$ is much greater or smaller than $T$ (periodicity of $S_T$), R(t) is modulated by either $S_T$ or $\dot{S}_T$, respectively (Heimisson and Avouac, 2020). In other words, whether R(t) is correlated by $S_T$(t) or $\dot{S}_T$(t) depends on the relative duration between $t_a$ and $T$. This finding appears to explain tectonic tremors modulated by daily tidal stress along the San Andreas Fault and similar tectonic settings because $t_a >> T$ in this setting (Beaucé et al., 2023; Bucholc and Steacy, 2016; Thomas et al., 2009), whereas microseisms are modulated by seasonal loading stress rate in California, the Himalayas, and the Azores and thus $t_a << T$ there (Bettinelli et al., 2008; Johnson et al., 2017; Lordi et al., 2022). However, it's difficult to observe periodic stress modulated seismicity along terrestrial faults because our observations are typically much shorter than an earthquake cycle (Beeler and Lockner, 2003).

Ice shelves are large floating pieces of ice which are fed by continental ice flowing onto the ocean. Due to this floatation, seismicity (i.e. icequakes) on ice shelves has been shown to be strongly tidally modulated and periodic (Anandakrishnan and Alley, 1997; Cole, 2020; Huang et al., 2022; Lucas et al., 2023; Minowa et al., 2019; Olinger et al., 2019; Olsen et al., 2021; Podolskiy et al., 2016), making ice shelf seismicity ideal to study the relationship between periodic oscillatory stress, characteristic time, and seismicity. Within an ice shelf, seismicity can occur along large rifts (Cole, 2020). These rifts are formed due to the extensional flow of the ice shelf towards the ocean (Walker and Gardner, 2019). Although on long time periods ice shelf flow is dominantly ductile deformation, rifts, crevasses, and other fractures observed in satellite imagery are evidence of brittle deformation that have undergone repeated periods of growth and quiescence (Walker and Gardner, 2019). Similar to the active plate margins, it is therefore reasonable to assume that each rift system has a background stress rate, and fractures along rifts are similar to earthquakes along faults. Therefore, seismicity along rifts is an ideal setting for testing brittle behavior under periodic stress loading in the rate-and-state friction framework.

In this study, we use a joint seismic and geodetic deployment on the Ross Ice Shelf (RIS) from the DRRIS project (Bromirski et al., 2015; Bromirski and Gerstoft, 2017) to test the rate-and-state periodic stress model (Eq. (2)), investigate the brittle deformation of rifts, and determine how fault maturation influences the characteristic time and overall strength of rifts under oscillatory stress. The DRRIS project was a RIS-wide geophysics deployment, including seismic and GPS stations near two large mid ice shelf rifts, Western Rift 4 and 6 (WR4 and WR6) (Fig. 1a). They are part of a series of periodically spaced rift zones that are proposed to be formed by the same mechanism (Walker et al., 2013; Walker and Gardner, 2019). WR6 was first observed in satellite imagery in 1975, and WR4 was formed 45–50 years prior to WR6. There is no evidence of active lateral propagation in WR4, whereas a rapid rift-tip propagation is observed for WR6 (Walker and Gardner, 2019). Upon examination of the satellite imagery presented in Walker and Gardner (2019), we found that the portion of WR6 that was instrumented during the DRRIS deployment was formed between 2004–2008, implying it was between 6–10 years old at the time of the deployment. This allows us to compare behaviors between a mature rift, WR4, and a juvenile rift, WR6. We can thus demonstrate how seismology can be used to observe and characterize the brittle failure process of ice and constrain time-evolving properties of ice rifts.

## 2. Data and methods

### 2.1. Seismic and GPS data

We utilized seismic catalogs (DR13, DR14, and DR15) for the mature and the juvenile rifts based on a STA/LTA (short-time-average through long-time-average trigger) approach by Olsen et al. (2021) with seismic records from DRRIS (Bromirski et al., 2015; Bromirski and Gerstoft, 2017), allowing for analysis and comparisons of the seismicity between the two rifts. Station DR15 is located ∼8 km north of the juvenile rift, and stations DR13 and DR14 are located ∼3 km and ∼7 km south and north of the mature rift, respectively (Fig. 1a). Because of the significantly closer proximity of DR14 to the mature rift compared to DR15 to the juvenile rift, caution must be taken when comparing seismicity detected by the two stations. As DR13 and DR15 have similar distances from their respective rift zones, the difference of icequake numbers should be mainly due to their seismogenic signatures. The available seismic records are ∼25 months long. There are several data gaps for DR13, so we only utilize a continuous portion of the record from 03/23/2016 to 11/10/2016 for the analysis. The seismic catalog of the mature and juvenile rifts is from three seismic records: the full DR14 record (12,986 events), the full DR15 record (4,199 events), and the cropped DR13 record (1,757 events). On average, the mature rift had 17.3 events per day (as recorded by DR14) and the juvenile rift had an average of 5.9 events per day (as recorded by DR15).

We additionally utilize the GPS data that were deployed during the same time period as the seismic stations, some of which were collocated with the seismic stations. The 3-component continuous GPS time series records were processed into 30-second sampling rate by Klein et al. (2020). GPS stations used in this study are shown as white circles in

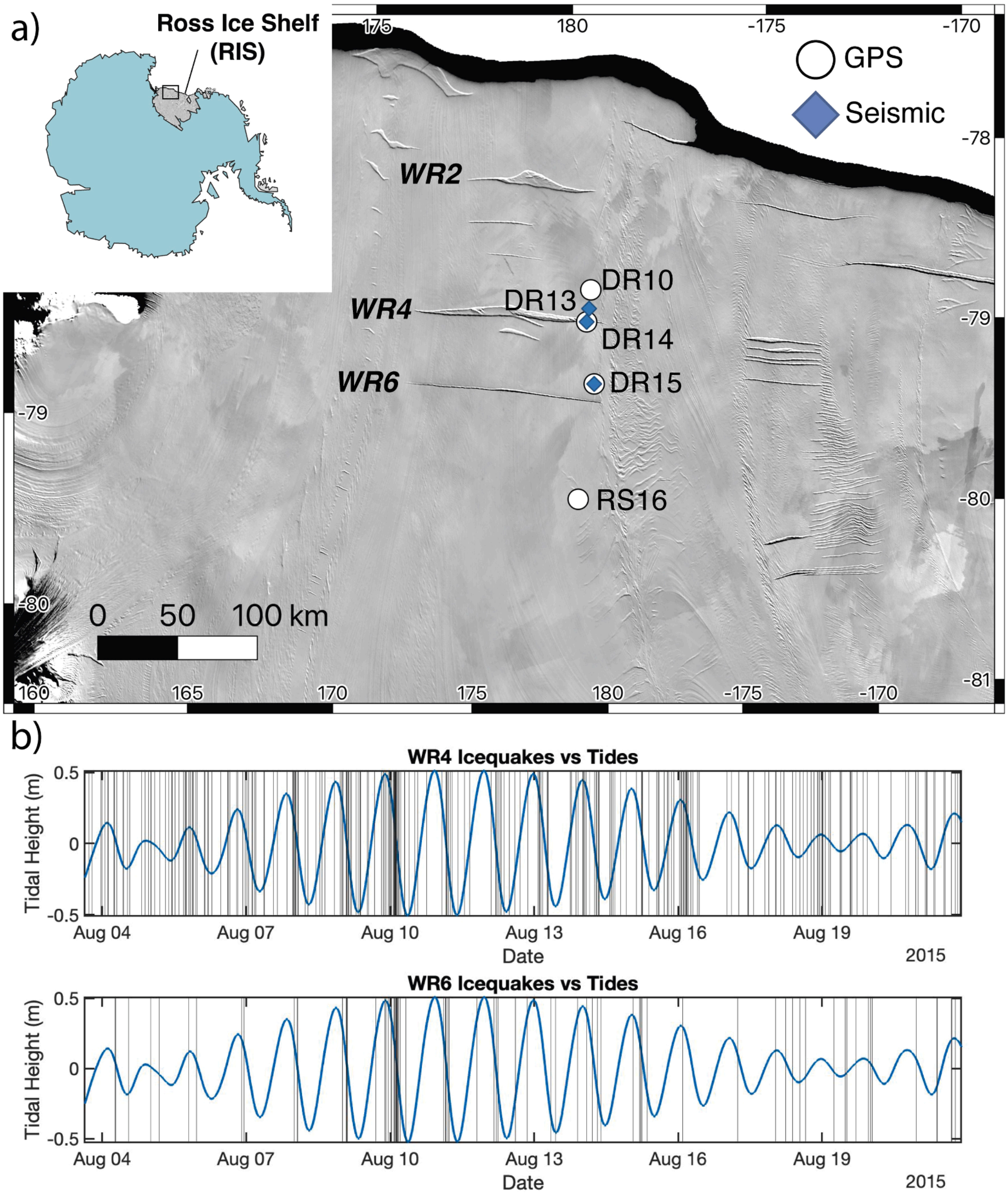


**Fig. 1.** (a) Map of the study region including the three WR rifts, WR2, WR4, WR6. Seismic stations from DRRIS used in this work are shown as blue diamonds (Bromirski et al., 2015; Bromirski and Gerstoft, 2017), and the GPS stations used in this work are shown as white circles (Klein et al., 2020). Background image is from MODIS. (b) Icequakes along WR4 (mature rift) (top) and WR6 (juvenile rift) (bottom) against modeled tidal height at each rift. Individual icequake events are shown as vertical black lines and the tidal height is shown in blue. The icequake catalog is based on (Olsen et al., 2021).

Fig. 1a with the same naming convention as for the seismic stations. We used DR10, DR14, DR15, and RS16 for our analysis due to their proximity to the rift zones. All the GPS stations with the exception of DR10 were operated using solar power, leading to data gaps during the austral winter (between April and September).

### 2.2. The Schuster test

This test has been used on terrestrial earthquakes to determine periodicity within an earthquake record (Ader and Avouac, 2013; Cochran et al., 2004; Tanaka et al., 2002). The test evaluates the likelihood that variations in the number of events observed over a test period can be due to random variations. The Schuster Spectrum can be affected by non-periodic distributions in the seismicity rates such as seismicity related to anthropogenic activities (Pearson, 2021), seismic swarms, and main-shock-aftershock sequences (Ader and Avouac, 2013). Through synthetic tests, Ader and Avouac (2013) further demonstrated that Schuster Spectrum only shows one significant period when the input seismic rate is purely sinusoidal, and a series of higher frequency harmonics when the input signal has mixed periodicities. The minimum period of these significant harmonics indicates the duration of the elevated seismic period for the non-sinusoidal periodic seismic rate. For example, for seismicity rate as a boxcar signal, the minimum harmonic period represents the width of the boxcar (Supplementary Fig. 1.3). We use the Schuster Spectrum algorithm developed by Ader and Avouac (2013) to analyze the periodicity of our seismic catalogs.

### 2.3. Stress and stress rate calculation

Tidal variations of sea level cause tilting of the ice shelf, which produces both extensional and compressional stresses with falling or rising tides, respectively (Bassis et al., 2008). Based on the CATS2008 tidal model designed for the RIS (Howard et al., 2019), Olinger et al. (2019) and Olsen et al. (2021) proposed that icequakes along WR4 and WR6 are most sensitive to extensional stress across the rift due to seaward tilt during falling tides. In both studies, the value of the stress due to tilt is calculated based on a tidal elevation model. However, using a tidal model to calculate periodic stress ($S_T$) at rifts may not be ideal due to the inherent structural complexity between the ice shelf and the mélange, which is not accounted for in the tidal modeling.

We assessed the accuracy of the tidal model by using GPS data and the assumption of elastic behavior, in which the amplitudes of local stress and strain remain proportional and in phase. This assumption is consistent with some studies of the elastic response of ice shelves to tides (Bassis et al., 2008; Minowa et al., 2019; Vaughan, 1995). Additionally, it is justified because we estimate the characteristic Maxwell relaxation time of ice to be ~2.4 days, based on properties in Brunt and MacAyeal (2014). The relaxation time is more than twice as long as the diurnal tidal stresses, which implies a near in-phase motions between stress and strain. Other studies calculate the Maxwell time to be ~11 h (Ultee et al., 2020), which would introduce a 20° phase shift between stress and strain. This amount of phase shift does not significantly affect our stress estimates (Supplementary Fig. 5.1).

We compare the strain recorded by GPS stations across each rift against stretching stress due to tilt predicted by the CATS2008 tidal model (Howard et al., 2019). We find a substantial phase shift between these stress predictions (Olinger et al., 2019; Olsen et al., 2021) and GPS derived strain across rifts (Supplementary Fig. 2.1). This suggests that a direct use of tidal models for estimating stretching stresses may not be adequate for investigating seismicity-stress correlations.

Since most of the GPS records only cover summer months, we cannot directly use the GPS-based strain time series to compare with the full seismic catalogs. Therefore, we extend the stress time series by using a modified tilt calculation and the CATS2008 model that can best represent the strain time series at WR4 and WR6 for the GPS data gaps. Our goal was to find the locations (as points) on the ice shelf that can be used to calculate tilt induced tidal stress ($S_T$) which has a phase that is most closely matching to the cross-rift GPS strain time series. Through this method we do not expect to calculate value of $S_T$ but rather achieve an accurate phase estimate of $S_T(t)$ and $\dot{S}_T(t)$ across each rift to compare against icequake occurrence. The relative magnitude should be meaningful as the modeled $S_T(t)$ matches GPS strain time series during spring and neap tides (Supplementary Fig. 2.2–2.5). To calculate $S_T(t)$, we obtained tidal elevation for the duration of the seismic records using the CATS2008 tidal model for the circum-Antarctic Ocean (Howard et al., 2019). We utilized the tidal model to compute $S_T(t)$ associated with tides using the same tidal tilt calculation utilized by Olinger et al. (2019). To accomplish this, we computed the tidal model of the RIS over the time period when the GPS data is available and then computed $S_T(t)$ for every location relative to a reference GPS station location on the landward (i.e. south) side of either WR4 or WR6 (Supplementary Fig. 2.2–5). We first normalized each tidal stress (as $\widehat{S}_T(t)$) and GPS records and then calculated the misfits of each location relative to the GPS station on the other side of the rift (Supplementary Fig. 2.2–5). We computed the root-mean square misfits for all available GPS records and selected the average location on the RIS with minimum root-mean square misfit as the target location that can best represent $S_T(t)$ phase across the rift (Supplementary Table 1). We next extend the time periods to the full duration of each seismic catalog to calculate the $S_T(t)$ and $\dot{S}_T(t)$ time series. Because the quantity of $S_T$ is not physically determined, we describe $S_T(t)$ and $\dot{S}_T(t)$ as in percentages or normalized (as $\widehat{S}_T(t)$ and $\widehat{\dot{S}_T}(t)$).

### 2.4. Analytical calculation of seismicity rate

We next predict seismic periodicity using the rate-and-state model with periodic stress (Eqs. (2)–(4)). $S_T$ (oscillatory Coulomb stress) in Eq. (4) requires slip on faults (instead of a pure mode-I fracture opening), knowledge of the orientation of faults, sense of shear, and coefficient of friction. The seismic catalogs we use are produced from single stations. We therefore cannot reliably determine the stress or the fracture orientation of any given event; however, based on examination of satellite imagery of rift features, we expect shear motion to occur at these rifts. Rift features shown in Supplementary Fig. 4.1 also suggest that frictional processes are likely involved in fault slip. $S_T(t)$ estimated here is essentially in phase with periodic loading stress in a simple 1D setting. This simplification is valid because $S_T(t)$ is always in phase with tidally driven horizontal loading stresses regardless of the fault dip angle. Eq. (4) also requires a background stress rate ($\dot{s}_0$) term. Here we do not attempt to compute the magnitude of $\dot{s}_0$, but it is reasonable to assume a non-zero $\dot{s}_0$ in the rift zones due to their existence as primarily brittle features and based on the observation of an overall increased velocity of ice flow on the RIS from the Antarctic continental interior toward the oceans (Klein et al., 2020). Finally, we also do not know the value of the constitutive material parameter $A$ described in Eq. (1) because constraining the material properties of the rift ice is outside of the scope of this work.

Combining Eqs. (2–4) we get,

$$R(t) = r\frac{\exp\left(\frac{S_T(t)+\ \dot{s}_0 t}{A\sigma_0}\right)}{1+\ \frac{\dot{s}_0}{A\sigma_0}\int_0^t \exp\left(\frac{S_T(\tau)+\ \dot{s}_0 \tau}{A\sigma_0}\right)d\tau}. \tag{5}$$

The background seismicity rate ($r$) is the expected rate of icequake production during the observation period as defined in Dieterich (1994). As described earlier, we cannot easily quantify $S_T(t)$, $\dot{s}_0$, and $A\sigma_0$. We rewrite each term in terms of its amplitude and unit: $S_T = \xi\widehat{S}_T$, $\dot{s}_0 = \eta\widehat{\dot{s}_0}$, $A\sigma_0 = \gamma\widehat{A\sigma_0}$. Here $\xi$, $\eta$, and $\gamma$ are the amplitudes of unit Coulomb stress ($\widehat{S}_T$; unit: Pa), background stress rate ($\widehat{\dot{s}_0}$; unit: Pa s$^{-1}$), and initial normal stress ($\widehat{A\sigma_0}$; unit: Pa), respectively. We can then rewrite Eq. (5) to compute the predicted seismicity rate, $R_{pred}(t)$:

$$R_{pred}(t) = r\frac{\exp\left(\frac{\xi}{\gamma}\frac{\widehat{S}_T(t)}{\widehat{A\sigma_0}}+\frac{\eta}{\gamma}\frac{\widehat{\dot{s}_0}}{\widehat{A\sigma_0}}t\right)}{1+\frac{\eta}{\gamma}\frac{\widehat{\dot{s}_0}}{\widehat{A\sigma_0}}\int_0^t \exp\left(\frac{\xi}{\gamma}\frac{\widehat{S}_T(\tau)}{\widehat{A\sigma_0}}+\frac{\eta}{\gamma}\frac{\widehat{\dot{s}_0}}{\widehat{A\sigma_0}}\tau\right)d\tau} \tag{6}$$

Note that $t_a = \frac{A\sigma_0}{\dot{s}_0} = \frac{\gamma}{\eta}\frac{\widehat{A\sigma_0}}{\widehat{\dot{s}_0}}$. This revised form allows us to determine $R(t)$ and $t_a$ with only $r$ and the ratios between $\xi$, $\eta$, and $\gamma$. By choosing these ratios we can determine $t_a$ (as $\frac{\gamma}{\eta}$) and the time scale for the background stress to reach the peak oscillatory Coulomb stress (as $\frac{\xi}{\eta}$). With more details in Section 2.2, we can then constrain $\frac{\gamma}{\eta}$ and $\frac{\xi}{\eta}$ by comparing $R_{pred}(t)$ and the observed seismicity rate, or $R_{obs}(t)$.

### 2.5. Stress windows

We additionally test how much the relative amount of stress and stress rate influences seismicity levels. Although icequakes typically exhibit a correlation with diurnal tides, main-shock-aftershock sequences appear more prominent during winter months (Chen et al., 2019; Huang et al., 2022; Olinger et al., 2019) and may potentially bias the analysis of stress modulation. Because this seismic dataset was produced by a single seismic station, we cannot easily apply common declustering methods due to unknown aftershock locations. To better examine tidal modulation without this type of influence, we follow an analysis proposed by Beaucé et al. (2023) to assess stress and stress rate modulation without declustering the catalog. This analysis compares $\widehat{S}_T$ and $\widehat{\dot{S}_T}$ at the time of an icequake to the relative frequency of the same $\widehat{S}_T$ and $\widehat{\dot{S}_T}$ condition over the observation period. We first break stress (or stress rate) into bins of 5 % width and define the proportion of icequakes that occur at a specific stress bin, $P_{IQ}(\widehat{S}_{Ti})$ (or stress rate bin, $P_{IQ}(\widehat{\dot{S}_{Ti}})$) within an observation period. We also define the proportion of duration of a specific stress bin (or stress rate bin) relative to the total duration of the observation period as $P_{\hat{S}_{Ti}}$ (or $P_{\hat{\dot{S}}_{Ti}}$). As suggested by Beaucé et al. (2023), we use a 28-day window with a 27-day overlap between each window to scan through the entire seismic record. We compute the icequake to stress ratio, Ψ (or stress rate ratio, $\dot{\Psi}$) for that time window:

$$\Psi = \frac{P_{IQ}(\widehat{S}_{Ti})}{P_{\hat{S}_T}} \text{ or } \dot{\Psi} = \frac{P_{IQ}(\widehat{\dot{S}_{Ti}})}{P_{\hat{\dot{S}}_T}}. \quad (7)$$

We iteratively repeat this process across the full duration of each seismic catalog and determine the median ratio for each stress and stress rate over all time windows. The median ratios for all time windows are $\Psi_\Sigma$ and $\dot{\Psi}_\Sigma$. This approach can reduce the effect of main-shock-aftershock sequences and allows for the relationship between events and $\widehat{S}_T$ or $\widehat{\dot{S}_T}$ to be more clearly assessed. If events are randomly distributed throughout the record, $\Psi_\Sigma$ or $\dot{\Psi}_\Sigma$ will be close to one. When events are reduced or enhanced during specific $\widehat{S}_T(t)$ or $\widehat{\dot{S}_T}(t)$ conditions, $\Psi_\Sigma$ or $\dot{\Psi}_\Sigma$ is less or greater than one, respectively. Further details about our stress window design choices and process are illustrated in Supplementary Fig. 3.1.

## 3. Results

To analyze the relationship between seismicity and tidal stress, we utilize seismic event records from three stations and GPS records from four stations deployed from 2014–2017 (Fig. 1a) (Klein et al., 2020; Olsen et al., 2021). By assuming that stress and strain across each rift are in phase on tidal timescales based on the viscosity of ice (see Supplementary Figs. 2.2–2.5 and 5.1), we compute a tidal stress model for each rift based on the phase of strain calculated from GPS across each rift. This results in a nondimensional stress record that captures amplitude change due to multi-component tidal variations such as larger spring tides. We are then able to compare the observed seismicity to the tidal stress conditions at each rift.

### 3.1. Periods of elevated seismicity

We first quantify the periodicity of seismicity in rifts by performing Schuster spectrum tests. The Schuster spectrum examines the probability that a periodicity observed in an earthquake catalog at a given set of periods is due to random chance. It is commonly applied to terrestrial seismic records (Ader and Avouac, 2013; Schuster, 1897). The Schuster spectrums for the two seismic catalogs are shown in Fig. 2. Additional results for the second seismic record at the mature rift recorded by station DR13 are shown in Supplementary Figure 3 and are consistent with results from the primary seismic record from station DR14. Seismicity at both rifts shows highly statistically significant periodicity at 24 h, the same period as the dominant diurnal tide. Additionally, both rifts have elevated seismicity levels over a period lasting ~6 h for the mature rift and ~3 h for the juvenile rift. In order to assess the robustness of our results, we repeat the Schuster spectrum tests on both catalogs after contaminating them with increasing numbers of random events (Supplementary Fig. 1.1) as well as with catalogs in which the event times are fully randomized (Supplementary Fig. 1.2). As expected, the fully randomized record shows no significant period and the catalogs with added noise maintain significance over the same periods as the original catalogs. Therefore, we conclude that seismicity at both rifts occurs periodically in response to diurnal tide influence.

### 3.2. Timing of seismicity relative to stress and stress rate

We predict seismic periodicity using a modified rate-and-state model with periodic stress (Eq. (5)). To do this, we first estimate $R_{pred}$ by varying $\frac{\xi}{\eta}$ and $\frac{\gamma}{\eta}$ in Eq. (6) as a grid search and then compare with observed seismicity rate ($R_{obs}$) by calculating the variance reduction ($VR$ (%) $= \left[1 - \sum_i (R_{obs\,i} - R_{pred_i})^2 / \sum_i (R_{obs\,i})^2\right] \times 100$). We hold $\gamma$ to be constant (as $10^{-6}$) based on an order of magnitude estimation measured by the GPS (Klein et al., 2020). We can finally estimate $t_a$ based on the highest achieved VR. Fig. 3 shows the VR of $R_{pred}(t)$ and the corresponding $t_a$ with different stress and stress rate parameters. The VRs are 98.5 % and 93.8 % from these grid searches for the mature and juvenile rifts respectively (Fig. 3a and b). The calculated best fitting $t_a$ is 1.93 h (0.31 to 3.22 h within 99th percentile range) for the mature rift and 2.78 h (0.79 to 5.15 h within 99th percentile range) for the juvenile rift. The mature rift has a wider range of high VR than the juvenile rift, and additionally the juvenile rift has the best fit with a higher $\frac{\xi}{\eta}$, or $\frac{S_T(t)}{\dot{s}_0}$,

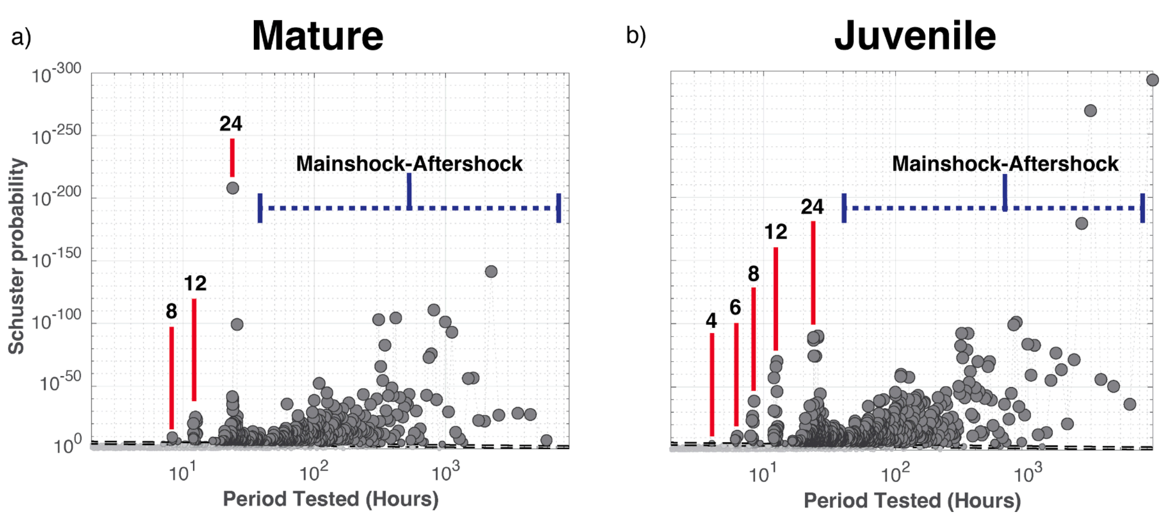


**Fig. 2.** (a and b) The results of the Schuster Spectrum on the seismic records. The most significant period for each record is ~24 h, corresponding to daily tidal cycles. Each record indicates mainshock-aftershock sequences, shown by higher amplitudes towards longer periods, labeled by the dark blue dotted line. Harmonics of 24 h also appear, indicating a non-sinusoidal periodic seismicity rate (Ader and Avouac, 2013). Note that the probabilities on the y-axis are shown as small values, because they measure the probability the period tested would occur in a randomly distributed seismic catalog.

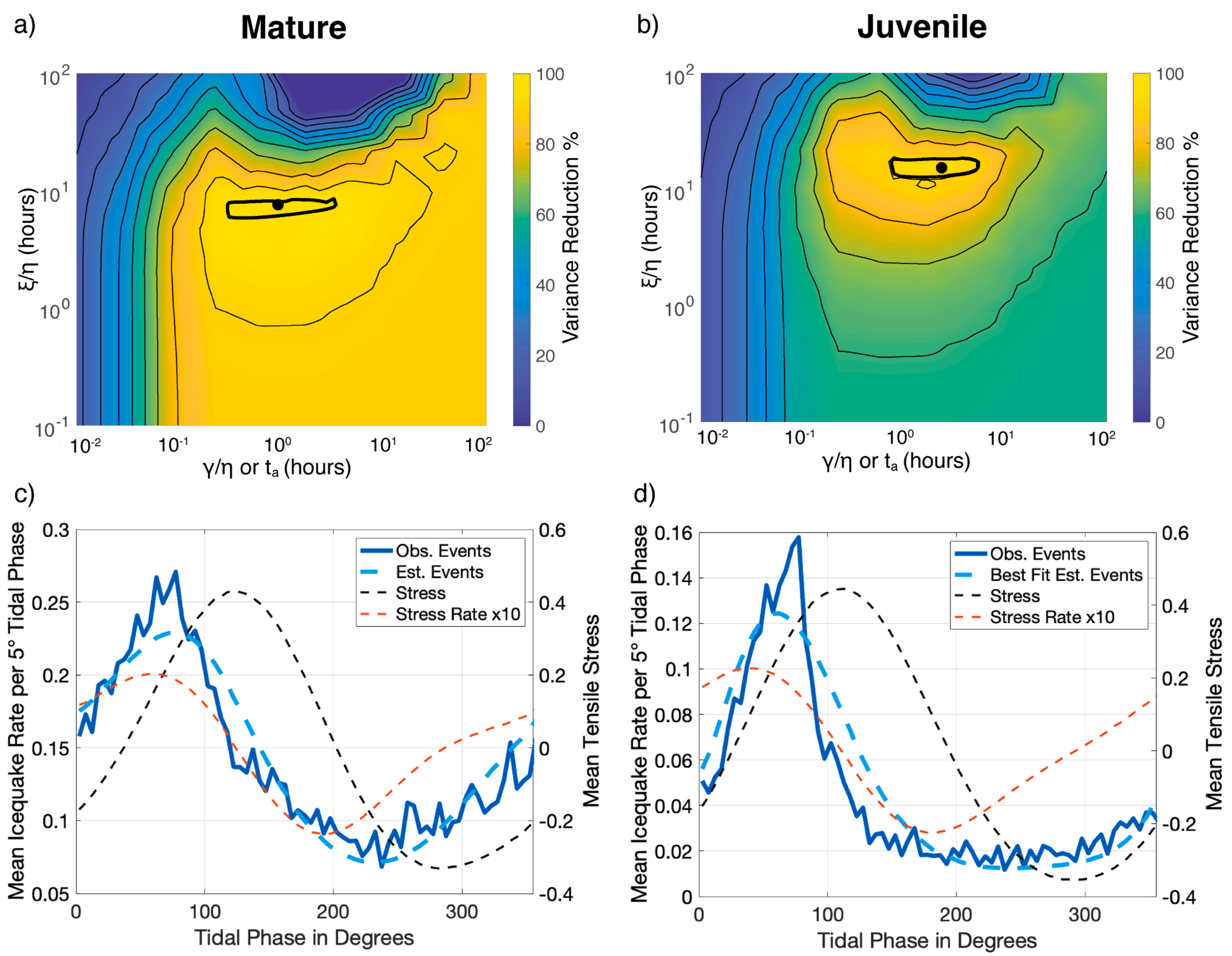


**Fig. 3.** (a and b) Variance reduction (VR) of predicted seismicity rate ($R_{pred}(t)$) with different $\frac{\xi}{\eta}$ and $t_a$. The black circles indicate the best fit $\frac{\xi}{\eta}$ and $t_a$ values. The thick contour represents the 99th percentile VR out of all VR achieved. The thin contours are at every 10 % VR. (c, d) $R_{pred}(t)$ (light blue dotted line) with the highest VR for the mature and juvenile rifts. The periodic stress and stress rates are shown as black and orange dotted lines, respectively. $R_{obs}(t)$ is shown in dark blue solid line. The full record of all values was stacked over a 360° tidal phase and averaged per 5° phase bin. Note the scales for icequake rate are different between (c) and (d).

the proportion of oscillating Coulomb stress relative to the background stress rate. This proportion describes the amount of time it takes for the background stress to reach the same level of the peak oscillatory coulomb stress. The best fitting $\frac{\xi}{\eta}$ is 7.61 h (6.02 to 8.55 h within 99th percentile range) for the mature rift and is 15.36 h (13.66 to 17.27 h within 99th percentile range) for the juvenile rift. The juvenile rift having a larger $\frac{\xi}{\eta}$ likely implies that the background stress rate in this area is lower than in the area of the mature rift. This could be due to an increased ice flow rate (i.e. higher background stress rate) toward the front of the ice shelf (Klein et al., 2020). The seismicity at the rifts is mainly in phase with the tidal stress rate. The estimated seismicity of the mature rift was closer in phase to the stress rate than the estimated seismicity of the juvenile rift, indicating a stronger modulation with stress rate for the mature rift (Fig. 3c and d). We find that the rate and state periodic model is able to accurately predict the observed seismicity rate given only a normalized stress model and observed background seismicity rate. As Huang et al. (2022) postulated most icequakes observed at the mature rift are shallow, we suggest that at least the shallow portion of the ice shelf fractured due to diurnal tidal stresses can recover on timescales shorter than a day and likely on the scale of hours, similar to the $t_a$ estimation in Fig. 3.

### 3.3. Quantity of seismicity relative to amount of stress and stress rate

Since seismicity at both rifts is primarily driven by stress rate, we further test the relationship between the number of seismic events to the magnitude of stress rate relative to the maximum absolute stress rate.

We perform this stress window method for all seismic catalogs and both stress and stress rate (Fig. 4a–d and Supplementary Fig. 3.2). We find that seismicity depends exponentially on the absolute stress rate, with a slight dependence on the absolute stress amount (Fig. 4a–d and Supplementary Table 2). To better demonstrate their exponential dependence, we used an L2 norm fit to each dataset to an exponential function with weighting based on the distribution of each ratio bin. This exponential relationship is:

$$\Psi_\Sigma(\widehat{\dot{S}_T}) = \Psi_\Sigma|_{\dot{S}_T=0}\, e^{b\hat{\dot{S}}_T}, \quad (8)$$

where $\Psi_\Sigma(\widehat{\dot{S}_T})$ is the median percentage of icequakes to percentage stress rate as a function of percent stress rate for all time windows, $\Psi_\Sigma|_{\dot{S}_T=0}$ is the median percentage of icequakes to percentage stress rate at zero percent stress rate, $b$ is the slope of the exponential relationship, and $\widehat{\dot{S}_T}$ is the percentage stress rate of the maximum absolute stress rate of

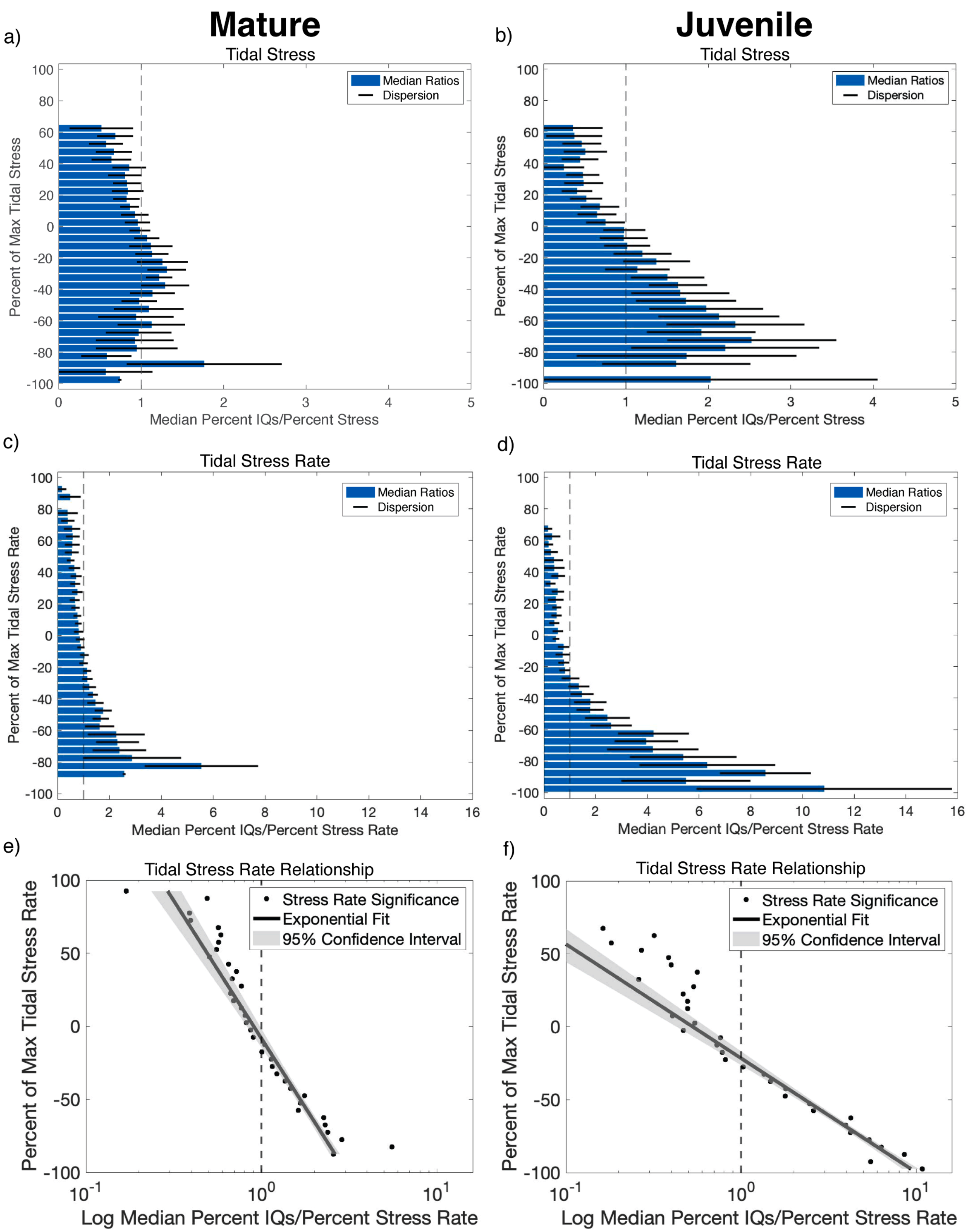


**Fig. 4.** (a–d) The vertical dashed lines indicate whether seismicity is positively related to tidal stress/stress rate (to the right of the line) or negatively related to tidal stress/stress rate (to the left of the line). Each bar represents the median ratio of percentage of icequakes to percentage of stress/stress rate within a given time window. The dispersion of these medians is shown by the horizontal black lines. Each bar is 5 % of the percentage of stress or stress rate interval. (e, f) Exponential fit to the bar plots in (c,d) (Eq. (8)). Note seismicity in the juvenile rift has a higher exponential dependence on stress rate with a $b$ of −0.012 for the mature rift and −0.029 for the juvenile rift.

the record. Additionally, the 95 % confidence interval was estimated for each fit (grey zone in Fig. 4e and f)).

The largest proportion of seismic events occur under the largest extensional stress rate conditions, which would correspond to spring tides. During periods when stress is becoming more compressional (i.e. positive stress rate), icequakes are suppressed with a smaller proportion of events occurring under these conditions. However, when fitting the ratios of proportion of seismic activity to proportion stress or stress rate using exponential function (Eq. (8)) (Fig. 4e and f), this model underpredicts the proportion of events under high compressional stress rate. This deviation from the exponential prediction may indicate the existence of an additional compressive stress related mechanism driving an excess number of events. At other ice shelves it has been found that basal icequake events can occur under rising tide, inferred to be extensional conditions at the base due to bending (Hammer et al., 2015; Minowa et al., 2019). The excess events we observe here may also be indicative of the existence of basal events, though we cannot determine this without accurate icequake event locations and depths.

### 3.4. Influence of rift maturity on seismicity

All of the above analyses indicate a difference in the behavior of a juvenile rift when compared to a mature rift. We find that the juvenile rift has a larger ratio between the magnitudes of oscillatory Coulomb stress and background stress rate, $\frac{\xi}{\eta}$, than the mature rift and that the size of $\frac{\xi}{\eta}$ influences the steepness of the estimated seismicity rate curve (Fig. 3c and d light blue dotted line). Because ice shelf dilatation rate increases closer to the ice shelf front, a lower background stress rate at the juvenile rift would show up as a higher $\frac{\xi}{\eta}$ if the magnitude of periodic stress between the rifts were approximately equal. Based on the Schuster spectrum and stress window analysis, seismicity at the juvenile rift is elevated over a shorter duration of time and has a larger exponential relationship between seismicity and relative stress rate magnitude (Figs. 2 and 3c and d).

The differences between the two rifts may be explained by age-related structural changes. Because the mature rift can fracture under lower relative magnitude stress rate and has a longer duration of elevated seismicity than the juvenile rift, we infer that matured rifts are more vulnerable to brittle fracture under proportionally lower stress rates. Additionally, we find that the range of $t_a$ between the two rifts has substantial overlap (Fig. 3a and b) but on average the $t_a$ of the juvenile rift is longer. From Eq. (1), both a higher $\dot{s}_0$ (background stress rate) and lower $A$ (inferred as material strength) can result in a lower $t_a$. A continuous dilatation and fracturing process can gradually decrease the strength of a mature rift compared to a juvenile rift and cause a lower $A$, which contributes to a lower $t_a$. Based on these differences, we additionally provide an estimation of the seismic rate of WR2, the most

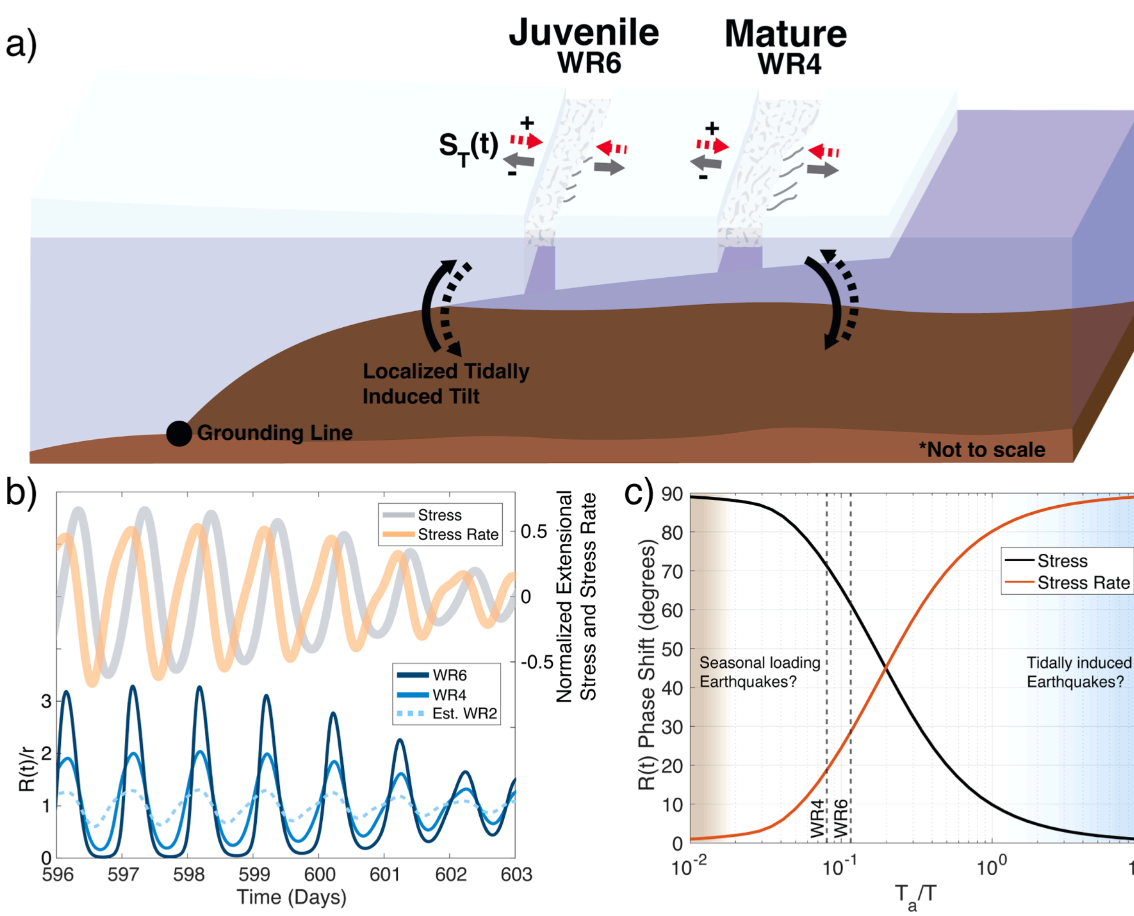


**Fig. 5.** (a) Schematic showing the RIS with WR4 and WR6 and the stresses applied to the rifts. Long-term background stress rate is shown with thick black arrows, periodic tidally driven stress is shown in red dotted (compressive) and black solid (extensional) arrows. Structural differences between WR4 and WR6 are shown by the gray fractures on the right of each rift. Arrows indicating the tidally induced ice shelf tilt are shown with the dotted line corresponding to the dotted periodic compressive stress and the solid line corresponding to extensional periodic stress. Schematic is not to scale. (b) Comparison between normalized extensional periodic stress (gray line) and stress rate (orange line) and the estimated $R(t)/r$ for each rift (WR6 dark blue line, WR4, blue line, estimated WR2 light blue dotted line). (c) Estimated $R(t)$ phase shift from either stress (black line) or stress rate (orange line) (in degrees) for each $T_a/T$ ratio. WR4 and WR6 $T_a/T$ are plotted to show their relative phase shifts. Zones where seasonal loading induced earthquakes (brown shading) and tidally induced earthquakes (blue shading) may fall are shown. Note that these curves were calculated using a simple sinusoidal period and so may be a simplification of the true phase shifts relative to $T_a/T$.

mature rift in the Western Ross series of rifts, relative to periodic stress and stress rate in Fig. 5b. Based on our results for WR4 (the mature rift) and WR6 (the juvenile rift), we would expect the seismicity rate of WR2 to have even higher modulation to stress rate due to its increased maturity.

From the surface features observed from Worldview satellite imagery, the mean fracture (interpreted as en échelon) length over a ~2.5 km segment near the instrumented portion of the juvenile rift is shorter (184 m) than that of a same length segment of the mature rift (285 m) (Supplementary Fig. 4.1). Additionally, the sinuosity of shorter fractures is greater for the mature rift than the juvenile rift. This may suggest that fracturing at the juvenile rift requires a higher activation periodic stress rate to develop new fractures while fracturing in the mature rift may mainly slide along pre-existing fractures within a more developed damaged zone. This type of behavior has been observed on terrestrial faults, where the maturity of the fault zone influences its seismicity (Thakur and Huang, 2021; Thomas et al., 2013). Further, similar to our findings about the relationship between $t_a$ and rift maturity, previous work has found that more mature terrestrial faults have lower aftershock production than juvenile faults (Guo et al., 2023). Despite having only two rifts to compare, our findings are in line with findings for terrestrial faults; the juvenile rift is more difficult to fracture, requiring higher relative stress rates for events to occur and having events occur over a shorter duration of elevated seismicity than the mature rift. We propose that this indicates that some sort of fatigue or damage zone process exists for ice rifts, which has also been observed for terrestrial faults and may have implications for ice shelf stability.

### 3.5. Broader applications

The applicability of this terrestrial model to seismicity along ice rifts implies that the model may be successfully used for other ice seismicity. On Earth, this model may be applied to other ice rift systems to determine expected seismicity. Cryoseismicity on ice rifts may be driven by the same fundamental processes as seismicity on terrestrial faults. Because these rifts exhibit shorter characteristic times implying a predominantly stress rate modulated seismicity rate, ice likely has a faster recovery rate than terrestrial faults allowing it to react on shorter timescales to stress changes. Due to the short duration and repetition of icequake cycles, low environmental noise level, and clear tidal modulation of events, cryoseismology may be helpful to provide insights into terrestrial seismology processes.

## 4. Discussion and conclusions

We apply a rate-and-state friction model to two Ross Ice Shelf rifts, one mature and one juvenile, to accurately calculate the expected seismicity rate for both. Through the application of this model, we determine the characteristic times ($t_a$) for each rift and find them to be shorter than the tidal stress period. This implies both rifts are more strongly modulated by tidally driven stress rate rather than tidal stress. Unlike terrestrial faults, our analysis indicates that ice has a relatively faster (less than a day) recovery time. We additionally find that the seismicity levels at both rifts are exponentially dependent on the magnitude of tidal stress rate applied to each system. When comparing the two rifts, the mature rift appears to fracture more easily as a larger proportion of events occurring at lower relative tidal stress rate levels and for a longer duration of elevated seismicity rate for each tidal cycle (Figs. 3 and 4). We suggest the differences in seismic response to stress rate between the mature and juvenile rifts may be due to a wider damage zone and well-established fractures surrounding the mature rift.

Because there is no direct estimate of stress for either rift system due to sparse instrumentation coverage, we instead calculated the tidal stress phase and relative amplitude based on a combined GPS and tidal model by assuming that rifts behave elastically on tidal timescales. However, future work containing GPS stations more closely positioned across a rift would allow for better strain phase and amplitude measurements. A multi-seismometer deployment would also allow for better stress assessment such as computing icequake moment tensors.

Rifts appear to be dominantly extensional features, which if the extension is accommodated through opening fracture, would limit the usage of this model for these systems. However, upon examination of the rift structures there is evidence for features produced by shear, implying the usage of a frictional model on these systems is reasonable (Supplementary Fig. 4.1). Considerations for whether an ice rift exhibits fracturing beyond opening fracture will need to be taken before applying this model to other ice rift systems. Future work may utilize seismic source modeling from higher resolution seismic data to resolve the mode of fracture occurring at these rifts. The best fitting results from applying this model to other rifts provides information on the material strength of the rift, the proportion of tidal stress to background stress rate, and the characteristic time of seismic events in the system. Additionally, including GPS to inform stress calculations allows us to accurately characterize regional differential tidal stress phases and better describe the modulation of seismicity to tidal stress rate. Our approach emphasizes the importance of including geodetic data in obtaining the full picture of tidally driven seismicity.

Through applying the rate-and-state model for seismicity driven by periodic stress to the two rifts, we verify the model's usage in a cryosphere setting while also validating the accuracy of the model in reproducing observed seismic rates for systems driven by periodic stresses such as tides. Our analysis both demonstrates that terrestrial seismology models can be accurately applied to ice shelf rift systems and that the rate and state periodic stress model is accurate in reproducing observed seismicity rates due to an oscillating stress such as tides. Our results suggest that rift seismicity is modulated by tidal stress rate and rifts may become easier to fracture as they mature. Understanding brittle fracture processes at rift zones contributes to the full picture of ice shelf deformation which is necessary for determining their stability under future climate conditions. Brittle failure of ice is also relevant to glacial fracture, specifically to hard to reach subglacial volcanic systems where icequake swarms are common (Ultee et al., 2020). Verifying the applicability and accuracy of the periodic rate and state model validates its usage, allowing for a deeper understanding of the earthquake cycle. Finally, this model may be useful for planetary applications. In particular, this model may be used for icy ocean moons such as Enceladus and Europa where tidally driven fracture is thought to occur (Hurford et al., 2020, 2007; Rhoden et al., 2015). Based on a tidal stress model, an assumed background seismicity rate, and expected material strengths, one could predict the times when the highest levels of seismicity are expected to occur on these moons, which may be critical information to future missions with a short lifespan.

## Funding

National Science Foundation Graduate Research Fellowship Program grant DGE 2236417 (KU)

National Science Foundation EAR-2026099 (MH)

NASA SSERVI GEODES grant 80NSSC19M0216 (VL)

## CRediT authorship contribution statement

**Kathrine Udell-Lopez:** Writing – review & editing, Writing – original draft, Visualization, Methodology, Investigation, Conceptualization. **Mong-Han Huang:** Writing – review & editing, Visualization, Supervision, Methodology, Investigation, Conceptualization. **Vedran Lekić:** Writing – review & editing, Visualization, Methodology, Conceptualization.

## Declaration of competing interest

The authors declare that they have no known competing financial interests or personal relationships that could have appeared to influence the work reported in this paper.


## Acknowledgments

This material is based upon work supported by the National Science Foundation Graduate Research Fellowship Program. Any opinions, findings, and conclusions or recommendations expressed in this material are those of the authors and do not necessarily reflect the views of the National Science Foundation. We appreciate feedback from Dr. Nicholas Schmerr and Dr. Terry Hurford on the direction of this work. We additionally appreciate the DRRIS project for their deployment and datasets. The seismic catalogs from the three seismic stations were generated by Dr. Kira Olsen based on Olsen et al. (2021). We thank the editor and an anonymous reviewer for their feedback which substantially improved the quality of this paper.


## Supplementary materials

Supplementary material associated with this article can be found, in the online version, at doi:10.1016/j.epsl.2025.119790.

## Data availability

Data will be made available on request.

## References


Ader, T.J., Avouac, J.-P., 2013. Detecting periodicities and declustering in earthquake catalogs using the Schuster spectrum, application to himalayan seismicity. Earth. Planet. Sci. Lett. 377–378, 97–105. https://doi.org/10.1016/j.epsl.2013.06.032.

Alley, R.B., Cuffey, K.M., Bassis, J.N., Alley, K.E., Wang, S., Parizek, B.R., Anandakrishnan, S., Christianson, K., DeConto, R.M., 2023. Iceberg calving: regimes and transitions. Annu Rev. Earth. Planet. Sci. 51, 189–215. https://doi.org/10.1146/annurev-earth-032320-110916.

Anandakrishnan, S., Alley, R.B., 1997. Tidal forcing of basal seismicity of ice stream C, West Antarctica, observed far inland. J. Geophys. Res.: Solid Earth 102, 15183–15196. https://doi.org/10.1029/97JB01073.

Bassis, J.N., Fricker, H.A., Coleman, R., Minster, J.-B., 2008. An investigation into the forces that drive ice-shelf rift propagation on the Amery Ice Shelf, East Antarctica. J. Glaciol. 54, 17–27. https://doi.org/10.3189/002214308784409116.

Beaucé, E., Poli, P., Waldhauser, F., Holtzman, B., Scholz, C., 2023. Enhanced tidal sensitivity of seismicity before the 2019 magnitude 7.1 Ridgecrest, California earthquake. Geophys. Res. Lett. 50, e2023GL104375. https://doi.org/10.1029/2023GL104375.

Beeler, N.M., Lockner, D.A., 2003. Why earthquakes correlate weakly with the solid Earth tides: effects of periodic stress on the rate and probability of earthquake occurrence. J. Geophys. Res.: Solid Earth 108. https://doi.org/10.1029/2001JB001518.

Beeler, N.M., Rubin, A., Bhattacharya, P., Kilgore, B., Tullis, T., 2022. Apparent age dependence of the fault weakening distance in rock friction. J. Geophys. Res.: Solid Earth 127, e2021JB022772. https://doi.org/10.1029/2021JB022772.

Bettinelli, P., Avouac, J.-P., Flouzat, M., Bollinger, L., Ramillien, G., Rajaure, S., Sapkota, S., 2008. Seasonal variations of seismicity and geodetic strain in the Himalaya induced by surface hydrology. Earth. Planet. Sci. Lett. 266, 332–344. https://doi.org/10.1016/j.epsl.2007.11.021.

Bromirski, P.D., Diez, A., Gerstoft, P., Stephen, R.A., Bolmer, T., Wiens, D.A., Aster, R.C., Nyblade, A., 2015. Ross ice shelf vibrations. Geophys. Res. Lett. 42, 7589–7597. https://doi.org/10.1002/2015GL065284.

Bromirski, P.D., Gerstoft, P., 2017. Dynamic Response of the Ross Ice Shelf to Wave-Induced Vibrations 2015/2016. https://doi.org/10.7283/58E3-GA46.

Brunt, K.M., MacAyeal, D.R., 2014. Tidal modulation of ice-shelf flow: a viscous model of the Ross Ice Shelf. J. Glaciol. 60, 500–508. https://doi.org/10.3189/2014JoG13J203.

Bucholc, M., Steacy, S., 2016. Tidal stress triggering of earthquakes in Southern California. Geophys. J. Int. 205, 681–693. https://doi.org/10.1093/gji/ggw045.

Chen, Z., Bromirski, P.D., Gerstoft, P., Stephen, R.A., Lee, W.S., Yun, S., Olinger, S.D., Aster, R.C., Wiens, D.A., Nyblade, A.A., 2019. Ross ice shelf icequakes associated with Ocean gravity wave activity. Geophys. Res. Lett. 46, 8893–8902. https://doi.org/10.1029/2019GL084123.

Cochran, E.S., Vidale, J.E., Tanaka, S., 2004. Earth tides can trigger shallow thrust fault earthquakes. Science (1979) 306, 1164–1166. https://doi.org/10.1126/science.1103961.

Cole, H.M., 2020. Tidally Induced Seismicity At the Grounded Margins of the Ross Ice Shelf, Antarctica - Proquest. Colorado State University.

Dieterich, J., 1994. A constitutive law for rate of earthquake production and its application to earthquake clustering. J. Geophys. Res.: Solid Earth 99, 2601–2618. https://doi.org/10.1029/93JB02581.

Dieterich, J.H., 1992. Earthquake nucleation on faults with rate-and state-dependent strength. Tectonophysics 211, 115–134. https://doi.org/10.1016/0040-1951(92)90055-B.

Dieterich, J.H., 1987. Nucleation and triggering of earthquake slip: effect of periodic stresses. Tectonophysics 144, 127–139. https://doi.org/10.1016/0040-1951(87)90012-6.

Dieterich, J.H., 1986. A model for the nucleation of earthquake slip. Earthquake Source Mechanics. American Geophysical Union (AGU), pp. 37–47. https://doi.org/10.1029/GM037p0037.

Dieterich, J.H., Kilgore, B., 1996. Implications of fault constitutive properties for earthquake prediction. Proc. Natl. Acad. Sci. U.S.A. 93, 3787–3794. https://doi.org/10.1073/pnas.93.9.3787.

Dieterich, J.H., Kilgore, B.D., 1994. Direct observation of frictional contacts: new insights for state-dependent properties. PAGEOPH 143, 283–302. https://doi.org/10.1007/BF00874332.

Guo, H., Lay, T., Brodsky, E.E., 2023. Seismological indicators of geologically inferred fault maturity. J. Geophys. Res.: Solid Earth 128. https://doi.org/10.1029/2023JB027096 e2023JB027096.

Hammer, C., Ohrnberger, M., Schlindwein, V., 2015. Pattern of cryospheric seismic events observed at Ekström Ice Shelf, Antarctica. Geophys. Res. Lett. 42, 3936–3943. https://doi.org/10.1002/2015GL064029.

Heimisson, E.R., Avouac, J.-P., 2020. Analytical prediction of seismicity rate due to tides and other oscillating stresses. Geophys. Res. Lett. 47. https://doi.org/10.1029/2020GL090827 e2020GL090827.

Heimisson, E.R., Segall, P., 2018. Constitutive law for earthquake production based on rate-and-State friction: Dieterich 1994 revisited. J. Geophys. Res.: Solid Earth 123, 4141–4156. https://doi.org/10.1029/2018JB015656.

Howard, S.L., Padman, L., Erofeeva, S., 2019. CATS2008: Circum-Antarctic Tidal Simulation Version 2008. https://doi.org/10.15784/601235.

Hsu, Y.-J., Kao, H., Bürgmann, R., Lee, Y.-T., Huang, H.-H., Hsu, Y.-F., Wu, Y.-M., Zhuang, J., 2021. Synchronized and asynchronous modulation of seismicity by hydrological loading: a case study in Taiwan. Sci. Adv. 7, eabf7282. https://doi.org/10.1126/sciadv.abf7282.

Huang, M.-H., Udell Lopez, K., Olsen, K.G., 2022. Icequake-magnitude scaling relationship along a rift within the Ross Ice Shelf, Antarctica. Geophys. Res. Lett. 49. https://doi.org/10.1029/2022GL097961 e2022GL097961.

Hurford, T.A., Helfenstein, P., Hoppa, G.V., Greenberg, R., Bills, B.G., 2007. Eruptions arising from tidally controlled periodic openings of rifts on Enceladus. Nature 447, 292–294. https://doi.org/10.1038/nature05821.

Hurford, T.A., Henning, W.G., Maguire, R., Lekic, V., Schmerr, N., Panning, M., Bray, V. J., Manga, M., Kattenhorn, S.A., Quick, L.C., Rhoden, A.R., 2020. Seismicity on tidally active solid-surface worlds. Icarus 338, 113466. https://doi.org/10.1016/j.icarus.2019.113466.

Johnson, C.W., Fu, Y., Bürgmann, R., 2017. Seasonal water storage, stress modulation, and California seismicity. Science (1979) 356, 1161–1164. https://doi.org/10.1126/science.aak9547.

Klein, E., Mosbeux, C., Bromirski, P.D., Padman, L., Bock, Y., Springer, S.R., Fricker, H. A., 2020. Annual cycle in flow of Ross Ice Shelf, Antarctica: contribution of variable basal melting. J. Glaciol. 66, 861–875. https://doi.org/10.1017/jog.2020.61.

Lordi, A.L., Neves, M.C., Custódio, S., Dumont, S., 2022. Seasonal modulation of oceanic seismicity in the azores. Front. Earth. Sci. 10. https://doi.org/10.3389/feart.2022.995401.

Lucas, E.M., Nyblade, A.A., Aster, R.C., Wiens, D.A., Wilson, T.J., Winberry, J.P., Huerta, A.D., 2023. Tidally modulated glacial seismicity at the foundation Ice Stream, West Antarctica. J. Geophys. Res.: Earth Surf. 128. https://doi.org/10.1029/2023JF007172 e2023JF007172.

Minowa, M., Podolskiy, E.A., Sugiyama, S., 2019. Tide-modulated ice motion and seismicity of a floating glacier tongue in East Antarctica. Ann. Glaciol. 60, 57–67. https://doi.org/10.1017/aog.2019.25.

Olinger, S.D., Lipovsky, B.P., Denolle, M.A., 2024. Ocean coupling limits rupture velocity of fastest observed ice shelf rift propagation event. AGU Adv. 5. https://doi.org/10.1029/2023AV001023 e2023AV001023.

Olinger, S.D., Lipovsky, B.P., Wiens, D.A., Aster, R.C., Bromirski, P.D., Chen, Z., Gerstoft, P., Nyblade, A.A., Stephen, R.A., 2019. Tidal and thermal stresses drive seismicity along a major Ross Ice Shelf rift. Geophys. Res. Lett. 46, 6644–6652. https://doi.org/10.1029/2019GL082842.

Olsen, K.G., Hurford, T.A., Schmerr, N.C., Huang, M.-H., Brunt, K.M., Zipparo, S., Cole, H.M., Aster, R.C., 2021. Projected seismic activity at the tiger stripe fractures on Enceladus, Saturn, from an analog study of tidally modulated icequakes within the Ross Ice Shelf, Antarctica. J. Geophys. Res.: Planet. 126. https://doi.org/10.1029/2021JE006862 e2021JE006862.

Parsons, T., 2002. Global Omori law decay of triggered earthquakes: large aftershocks outside the classical aftershock zone. J. Geophys. Res.: Solid Earth 107. https://doi.org/10.1029/2001JB000646. ESE 9-1-ESE 9-20.

Pearson, K.M., 2021. Analyzing Time-Varying Seismicity and Aftershock Behavior in Central and Eastern United States. Doctoral dissertation. University of Maryland, College Park. https://doi.org/10.13016/hcom-tzjz.

Perfettini, H., Avouac, J.-P., 2004. Postseismic relaxation driven by brittle creep: a possible mechanism to reconcile geodetic measurements and the decay rate of aftershocks, application to the Chi-Chi earthquake, Taiwan. J. Geophys. Res.: Solid Earth 109. https://doi.org/10.1029/2003JB002488.

Podolskiy, E.A., Sugiyama, S., Funk, M., Walter, F., Genco, R., Tsutaki, S., Minowa, M., Ripepe, M., 2016. Tide-modulated ice flow variations drive seismicity near the

calving front of Bowdoin Glacier, Greenland. Geophys. Res. Lett. 43, 2036–2044. https://doi.org/10.1002/2016GL067743.
Rhoden, A.R., Hurford, T.A., Roth, L., Retherford, K., 2015. Linking Europa's plume activity to tides, tectonics, and liquid water. Icarus 253, 169–178. https://doi.org/10.1016/j.icarus.2015.02.023.
Rist, M.A., Sammonds, P.R., Murrell, S.a.F., Meredith, P.G., Doake, C.S.M., Oerter, H., Matsuki, K., 1999. Experimental and theoretical fracture mechanics applied to Antarctic ice fracture and surface crevassing. J. Geophys. Res.: Solid Earth 104, 2973–2987. https://doi.org/10.1029/1998JB900026.
Scambos, T., Fricker, H.A., Liu, C.-C., Bohlander, J., Fastook, J., Sargent, A., Massom, R., Wu, A.-M., 2009. Ice shelf disintegration by plate bending and hydro-fracture: satellite observations and model results of the 2008 Wilkins ice shelf break-ups. Earth. Planet. Sci. Lett. 280, 51–60. https://doi.org/10.1016/j.epsl.2008.12.027.
Schuster, A., 1897. On lunar and solar periodicities of earthquakes. Proc. R. Soc. Lond. 61, 455–465. https://doi.org/10.1098/rspl.1897.0060.
Stein, S., Liu, M., 2009. Long aftershock sequences within continents and implications for earthquake hazard assessment. Nature 462, 87–89. https://doi.org/10.1038/nature08502.
Tanaka, S., Ohtake, M., Sato, H., 2002. Evidence for tidal triggering of earthquakes as revealed from statistical analysis of global data. J. Geophys. Res.: Solid Earth 107. https://doi.org/10.1029/2001JB001577. ESE 1-1-ESE 1-11.
Thakur, P., Huang, Y., 2021. Influence of fault zone maturity on fully dynamic earthquake cycles. Geophys. Res. Lett. 48. https://doi.org/10.1029/2021GL094679 e2021GL094679.
Thomas, A.M., Bürgmann, R., Dreger, D.S., 2013. Incipient faulting near Lake Pillsbury, California, and the role of accessory faults in plate boundary evolution. Geology. 41, 1119–1122. https://doi.org/10.1130/G34588.1.
Thomas, A.M., Bürgmann, R., Shelly, D.R., Beeler, N.M., Rudolph, M.L., 2012. Tidal triggering of low frequency earthquakes near Parkfield, California: implications for fault mechanics within the brittle-ductile transition. J. Geophys. Res.: Solid Earth 117. https://doi.org/10.1029/2011JB009036.
Thomas, A.M., Nadeau, R.M., Bürgmann, R., 2009. Tremor-tide correlations and near-lithostatic pore pressure on the deep San Andreas fault. Nature 462, 1048–1051. https://doi.org/10.1038/nature08654.
Tolstoy, M., Vernon, F.L., Orcutt, J.A., Wyatt, F.K., 2002. Breathing of the seafloor: tidal correlations of seismicity at Axial volcano. Geology 30, 503–506. https://doi.org/10.1130/0091-7613(2002)030<0503:BOTSTC>2.0.CO;2.
Ueda, T., Kato, A., Johnson, C.W., Terakawa, T., 2024. Seasonal modulation of crustal seismicity in northeastern Japan driven by snow load. J. Geophys. Res.: Solid Earth 129. https://doi.org/10.1029/2023JB028217 e2023JB028217.
Ultee, L., Meyer, C., Minchew, B., 2020. Tensile strength of glacial ice deduced from observations of the 2015 eastern Skaftá cauldron collapse, Vatnajökull ice cap, Iceland. J. Glaciol. 66, 1024–1033. https://doi.org/10.1017/jog.2020.65.
Vaughan, D.G., 1995. Tidal flexure at ice shelf margins. J. Geophys. Res.: Solid Earth 100, 6213–6224. https://doi.org/10.1029/94JB02467.
Walker, C.C., Bassis, J.N., Fricker, H.A., Czerwinski, R.J., 2013. Structural and environmental controls on Antarctic ice shelf rift propagation inferred from satellite monitoring. J. Geophys. Res.: Earth Surf. 118, 2354–2364. https://doi.org/10.1002/2013JF002742.
Walker, C.C., Gardner, A.S., 2019. Evolution of ice shelf rifts: implications for formation mechanics and morphological controls. Earth. Planet. Sci. Lett. 526, 115764. https://doi.org/10.1016/j.epsl.2019.115764.